





Cite this: *Phys. Chem. Chem. Phys.*,
2020, 22, 4402

Energy landscape of Au₁₃: a global view of structure transformation†

Xiao-Tian Li,^{‡a} Shao-Gang Xu,^{‡a} Xiao-Bao Yang ^{ab} and Yu-Jun Zhao ^{*ab}

It has long been a challenge in physics and chemistry to acquire a global picture of the energy landscape of a specific material, as well as the kinetic transformation process between configurations of interest. Here we have presented a comprehensive approach to deal with the structure transformation problem, along with the illustration of the energy landscape, as exemplified with the case of Au₁₃. A configuration space based on interatomic distances was proposed and demonstrated to have a strong correlation between structure and energy, with application in structure analysis to screen for trial transition pathways. As several representative configurations and their transition pathways ascertained and by projecting on a plane, a visual two-dimensional contour map was sketched revealing the unique energy landscape of Au₁₃. It shows that the 2D and 3D clusters form two funnels in the high-dimensional configuration space, with a transition pathway with a 0.976 eV barrier bridging them.

Received 29th November 2019,
Accepted 27th January 2020

DOI: 10.1039/c9cp06463j

rsc.li/pccp

1 Introduction

In recent years, with the development of computer technology, a flurry of intelligent methods have been put forward in computational physics and chemistry for material prediction, including global optimization,^{1–4} high-throughput calculations,^{5,6} machine learning^{7,8} and so on. They focus on the configurations with excellent stabilities and novel properties for practical synthesis and applications. Beyond that, the kinetic transformation of the configurations is also of great importance for the guidelines of synthesis, but remains a challenge, especially for the transformation between two vastly different structures.

Setting aside traditional molecular dynamics and Monte Carlo, the kinetic properties can be derived from transition state theory,⁹ which turns the problem into searching for the minimum energy path (MEP) on the potential energy surface (PES). Nowadays, there are two classes of approaches widely used to locate the transition state (TS), the chain-of-states approaches like the nudged elastic band (NEB) method,^{10,11} and the surface walking approaches like the eigenvector following method¹² and the dimer method.¹³ The NEB method, for instance, locates the TSs by optimizing a chain of images simultaneously, which requires an initial reasonable pathway nearby.

In general, this is hard to set up aside from straightforward cases like diffusion processes and straightforward chemical reactions. As a result, methods like the transition path sampling^{14–16} and discrete path sampling¹⁷ were presented to acquire the important pathways from the ensemble, and was applied in the Lennard-Jones (LJ) clusters.

Besides, in the kaleidoscope of materials, there are typically thousands of atomic configurations to be dealt with, where an assortment of the structures is necessary. While the structures are typically located in a complicated high-dimensional configuration space, they should be projected to well-defined low-dimensional space for visual illustration. The disconnectivity graph,^{18,19} for example, is a wonderful strategy to project the structures into a one dimensional space with different threshold energies connecting them. Similarly, we have presented a novel eigen-subspace projection function (EPF) configuration space recently, on the basis of which the distribution and properties of LJ₃₈ clusters and boron sheets were studied.^{20,21} Besides the local minima, their kinetic transformations could also be taken into account to obtain a more detailed energy landscape. An efficient approach is thus presented here to screen for trial pathways between vastly different configurations for the NEB method, along with the illustration of the PES, as exemplified with an instance of gold clusters.

Small gold clusters up to the size of Au₂₆ have been recognized to have vastly different structures, evolving from planar shape, cagelike shape, pyramidal shape to tubular shape.^{22,23} Distinct from the analogs copper and silver, gold clusters at small sizes prefer to form planar structures, which is attributed to relativistic effects.^{24,25} Theoretical calculations predicted that neutral gold clusters form two-dimensional (2D) structures

^a Department of Physics and School of Materials Science and Engineering,
South China University of Technology, Guangzhou, Guangdong 510640, China.
E-mail: zhaoyj@scut.edu.cn; Fax: +86-20-87112837; Tel: +86-20-87110426

^b Key Laboratory of Advanced Energy Storage Materials of Guangdong Province,
South China University of Technology, Guangzhou, Guangdong 510640, China

† Electronic supplementary information (ESI) available. See DOI: 10.1039/c9cp06463j

‡ X.-T. L. and S.-G. X. contributed equally to this work.

up to Au₁₂, with the shape change from 2D to 3D at Au₁₃ and Au₁₄.^{26–28} As a result, gold clusters at the intermediate sizes such as Au₁₃ would have a variety of competitive configurations, including both 2D and 3D ones. The kinetic transformation between 2D and 3D Au₁₃ clusters turns out to be interesting, and was studied here by our pathway screening approach combined with the NEB method, with a visual 2D contour map sketched revealing the detailed energy landscape.

2 Methods

The trial pathways between two extremely different clusters, on the whole, can be determined in three steps: the atom correspondence, the orientation correspondence, and the detailed path. Among them, the atom correspondence is most important, and we qualify it by defining a metric, which, in a sense, quantifies the compatibility of the two clusters within the atom correspondence.

A commonly used distance between clusters p and q within certain atom correspondence can be defined by the root-mean-square (RMS) of the difference of their atomic coordinates

$$d_{\text{coord}}(p, q) = \frac{1}{\sqrt{n}} \min_{\mathbf{U}} \|\mathbf{R}_p - \mathbf{U}\mathbf{R}_q\|, \quad (1)$$

where $\mathbf{R} \equiv (r_1, r_2, \dots, r_n) \in \mathbb{R}^{3 \times n}$ stands for the atomic coordinates of a cluster with n atoms, and the absolute symbol represents taking the Frobenius norm for the coordinates of clusters p and q .²⁹ Here the centroids of the two clusters should be coincided beforehand, and then a rotation $\mathbf{U} \in \text{SO}(3)$ is operated on the cluster q to minimize the Frobenius norm. This is an orientation problem between two coordinate systems, and can be solved by the quaternion³⁰ or singular value decomposition (SVD)³¹ methods.

Since it is the distances between atoms that are of vital importance in physical interactions, a metric based on interatomic distances may contain essential structural characteristics related to the properties.³² A feasible distance between clusters p and q within certain atom correspondence can be defined by

$$d_{\text{dist}}(p, q) = \sqrt{\frac{2}{n(n-1)} \sum_{i=1}^{N-1} \sum_{j=i+1}^N (d_{p,ij} - d_{q,ij})^2}, \quad (2)$$

where d_{ij} is the Cartesian distance between atoms i and j in a cluster.

Although the two distances d_{coord} and d_{dist} can qualify the compatibility of two clusters within certain atom correspondence, we could not evaluate all the atom correspondences even for a small cluster with only 13 atoms due to the huge factorial amount. Here we selected the reasonable atom correspondences from the huge ensemble through two steps. First, for two clusters with the centroids coincided, rotate one of them by the three Euler angles (each from $2\pi/49$ to 2π), and then obtain the feasible atom correspondences by the Hungarian algorithm.³³ Second, for each feasible atom correspondence, exchange the order of two or three atoms ergodically for extensive atom orderings, until the best 200 ones converge with minimum d_{coord} or d_{dist} .

With the atom correspondences determined, the orientation correspondence of the two clusters could be obtained by the SVD method, and the detailed pathway could be achieved by simply linking the corresponding atoms. Such a pathway in fact is orthogonal to the manifolds of the two clusters swept by the rotation $\mathbf{U} \in \text{SO}(3)$, and turns out to be the shortest geometrical path with less frustration in transformation. In this way, the trial pathways were presented, which would be further optimized by the NEB method to the minimum.

First-principles calculations were performed here based on density-functional theory (DFT) with the projected augmented wave (PAW)³⁴ scheme, as implemented in the Vienna *ab initio* simulation package (VASP).³⁵ The spin-polarized generalized gradient approximations (GGA)³⁶ expressed by the Perdew–Burke–Ernzerhof (PBE) functional were employed for structure optimization. The energy cutoff was set to be 350 eV for the plane-wave basis set, and the unit cell was set to be $20 \text{ \AA} \times 20 \text{ \AA} \times 20 \text{ \AA}$ to eliminate the interactions between two neighboring clusters, with a K mesh of $1 \times 1 \times 1$. The convergence criteria of the force on each atom was 0.01 eV \AA^{-1} for the optimization. Following the trial pathways provided based on a configuration space, the climbing image nudged elastic band method (cNEB)¹¹ was adopted to optimize the transition pathways and states between the gold clusters, with the convergence of force on each atom less than 0.04 eV \AA^{-1} .

From the previous studies on Au clusters,^{26–28,37,38} we noticed that different functionals were used for the DFT calculations, which may lead to an intrinsic error bar. In particular, Assadollahzadeh *et al.*²⁸ had tested a lot of functionals and found that the nonlocal correlation functional provided by Perdew and Wang in 1991 (B3PW91)³⁹ is in good agreement with the precise all-electron calculations for the dipole polarizability of the gold atom.⁴⁰ Besides, Bulusu *et al.*³⁸ have examined the basis-set effects on the relative energies of Au _{n} ($n = 15–19$), and found that the PBE functional is suitable for the calculations. Following the work of Bulusu *et al.*,³⁸ we utilized the PBE functional for our study.

3 Results and discussion

We aimed at the low-lying landscape of Au₁₃ in this work. Firstly, we explored the most stable configurations for 2D and 3D structures separately. For the 2D configurations, we noticed that the most stable configurations are indeed planar triangular structures according to previous works.^{22,23,26–28} As a result, we have constructed all the planar triangular clusters (in total 328 ones), whose atoms have at least two neighboring coordinations (for stability consideration) by the EPF method.^{20,21} As for the 3D configurations, we explored the PES by a novel random method. We manipulated an image on the PES from one local minimum to a nearby local minimum by the adding of a pseudo-potential, which is a function of the distance (*e.g.* d_{dist}) to the initial local minima. After attaining a new local minimum, the Metropolis criterion was then utilized to decide whether to accept the new local minimum or not. We have attained more than 1500 3D configurations in total by the

random search method. All the 2D and 3D structures were then optimized precisely by the DFT calculations to the local minima, and the most stable structures were selected to construct a 2D projection map (see Fig. S1 in ESI†), showing the landscape of the Au₁₃ cluster.

In our calculations, we found that a 2D structure with C_s symmetry (set to 0 eV) turns out to be the most stable configuration, while a 2D structure with C_{2v} symmetry (0.026 eV) has the second best stability (see also Fig. 2). The 3D structures are indeed less stable than the 2D ones, and the most stable 3D structure with C_{3v} symmetry is 0.389 eV higher than the most stable 2D one in total energy. Our results are consistent with previous studies in general. For example, Xiao *et al.*²⁷ and Assadollahzadeh *et al.*²⁸ predicted that a 2D structure with C_{2v} symmetry is the most stable configuration, which turns out to be the second most energetically favored (0.026 eV) in our results. Besides, Xiao *et al.*²⁷ predicted that the most stable 3D structure is a structure with C_{3v} symmetry, and is ~0.39 eV higher than the most stable 2D structure, which are consistent with our results (with C_{3v} symmetry, 0.389 eV higher).

From the PES search of Au₁₃, we ascertained three representative configurations with the best stabilities for both the 2D and 3D structures. For each pair of the six configurations of Au₁₃, 10 trial pathways were generated by our pathway screening approach, and then optimized to the MEPs by the cNEB method. Much of them converge quickly (within 200 iterations), and the correlation between the barriers and distances are shown in Fig. 1, where the pathways are divided into three groups according to the structures of their initial and final states.

As expected, both d_{coord} and d_{dist} exhibit a strong correlation with the barrier, showing their abilities to screen for trial pathways. Among them, d_{dist} has a stronger correlation, especially for the 2D–2D transitions, with a larger correlation coefficient of 0.84 than 0.70 for d_{coord} . Indeed, a well-defined metric based on interatomic distances may reveal some essential characteristics for the structural transformation, like the d_{dist} . As shown in Fig. 1(b), the d_{dist} between 2D and 3D structures is apparently larger than that of 2D–2D and 3D–3D ones, in accordance with our intuition. These lead to the much larger barriers of 2D–3D transitions, showing the relevant role of d_{dist} in structural transformation.

With the most stable configurations and the transition pathways between them ascertained, a 2D contour map of the low-lying landscape of Au₁₃ was sketched, as shown in Fig. 2. The positions of configurations on the 2D map are determined by minimizing $\sum_{p,q} (d_{2D}(p,q) - d_{\text{dist}}(p,q))^2$, where $d_{2D}(p,q)$ is the distance of clusters p and q on the 2D map, while $d_{\text{dist}}(p,q)$ has taken into account all the atom correspondences to obtain the minimum distance. Naturally, $d_{\text{dist}}(p,q)$ is chosen here rather than $d_{\text{coord}}(p,q)$ for its stronger correlation with the PES.

In the schematic diagram, the 2D and 3D clusters are clearly separated, a good reflection of their structural differences. The 2D cluster region is apparently lower-lying than the 3D one, with the global minimum 2D-C_s-1 (0.000 eV) located at the

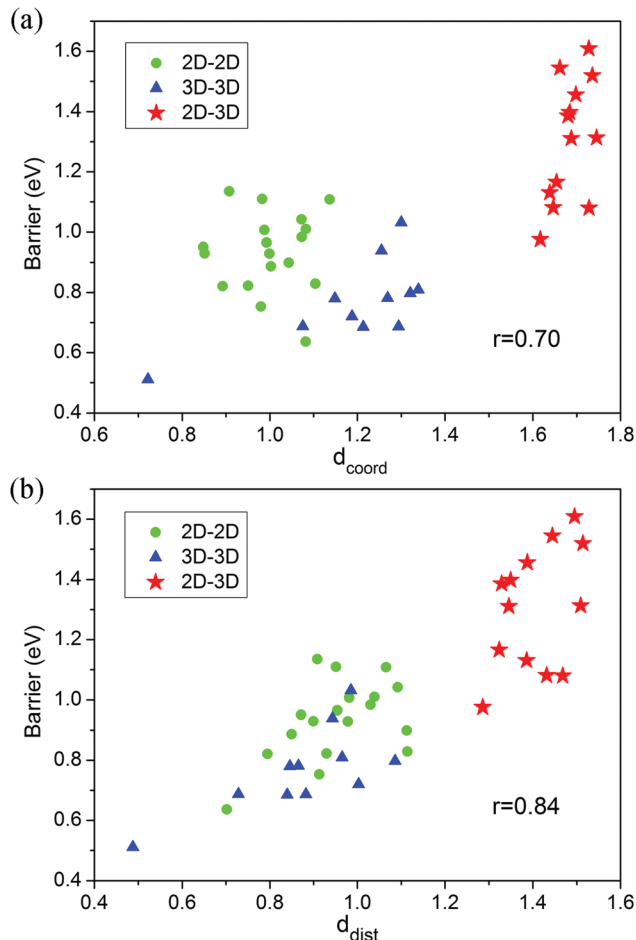


Fig. 1 Correlation of barriers and distances of the converged pathways of Au₁₃. The barriers are with respect to the global minimum 2D-C_s-1.

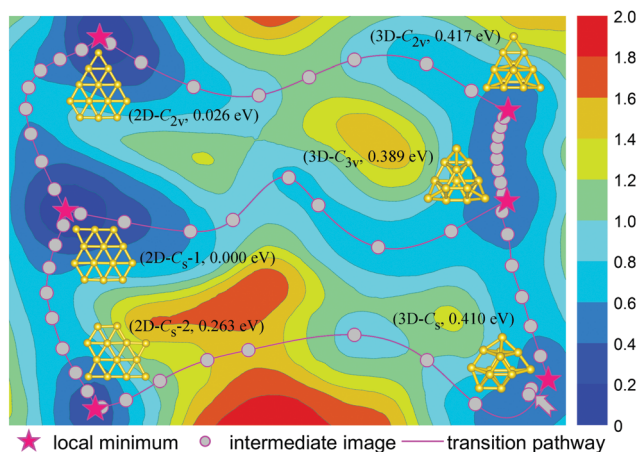


Fig. 2 2D contour map of the low-lying landscape of Au₁₃. The stars stand for six representative configurations with the best stabilities, with their detailed structures, notations and energies alongside, while the dots represent the intermediate images along the MEPs. The background color reflects the relative energies (in eV) with respect to the global minimum 2D-C_s-1, with the energies of the surrounding points achieved by interpolation.

middle left. In contrast, the 3D cluster region is about 0.4 eV higher, with the most stable 3D configuration 3D- C_{3v} (0.389 eV) located at the middle right. It is interesting that the 2D and 3D cluster regions separate not only in distance, but also in energy barrier, which has already been inferred by the foregoing distance–barrier correlation. As the contour map depicts, the 2D and 3D clusters get together due to their similar structures and lower barriers, forming two corrugated funnels in the high-dimensional configuration space with relatively higher barriers separating them.

Although the contour map well reflects the landscape of Au_{13} , there is, however, an “irregularity” with it when paying attention to the details. That is, the pathway between configurations 3D- C_{3v} and 3D- C_s on the lower right has two intermediate images alongside the path, as indicated by the arrow. By our further study, we found that the unforeseen irregularity is ascribed to the peculiar landscape around configuration 3D- C_s , a sandwich structure whose top and bottom layers are each constructed by three atoms in triangle, with seven interlayer atoms distributed around. Clearly, the interlayer atoms are insufficient to circle around entirely, with lack of an atom at the lower right. The corresponding inadequate bonding at the lower right thus leads to the instability of 3D- C_s , and by contrast, with an extra atom to provide completion, the perfect sandwich structure of Au_{14} exhibits outstanding stability and becomes more stable than the best 2D clusters, as shown in the ESI† (Fig. S2). That is why the structural mutation from 2D to 3D for gold clusters occurs at Au_{13} and Au_{14} .

Due to the insufficiency of interlayer atoms in 3D- C_s , there are, in fact, a series of sandwich configurations with different interlayers in shape. They have similar structures and comparable stabilities, forming a small corrugated basin on the PES, along with 3D- C_s . A contrasting contour map is provided in Fig. S3 (ESI†) in consideration of these sandwich configurations, revealing the detailed landscape around 3D- C_s . It shows that the pathway from 3D- C_{3v} towards 3D- C_s is influenced by the corrugated basin when passing through the sandwich structure SW1 (see the detailed pathway in Fig. S4, ESI†), leading to the irregularity in Fig. 2.

This can be also illustrated by the configuration scatter diagram in Fig. S1 (see ESI†). Unlike the other five structures (*i.e.* 2D- C_{2v} , 2D- C_s -1, 2D- C_s -2, 3D- C_{2v} , 3D- C_{3v}), the 3D- C_s is in fact deeply surrounded by many other local minima. As a result, the pathway from 2D- C_s -2 to 3D- C_s and the pathway from 3D- C_{3v} to 3D- C_s turn out to be complicated and flexuous, and thus are difficult to be set up. We need to consider the paths through local minima comprehensively, and achieve the actual pathway step by step.

With the overall PES of Au_{13} as illustrated in Fig. 2, it is now feasible to obtain the lowest pathway between 2D and 3D structures. Typically, the configurations 2D- C_s -1 and 3D- C_{3v} are relatively similar: 3D- C_{3v} is trigonal symmetrical with an atom at the center, while 2D- C_s -1 is approximately trigonal symmetrical with an atom projecting at the top left. As a result, the transition between 2D- C_s -1 and 3D- C_{3v} turns out to be easier compared with other 2D–3D transitions. As seen in Fig. 3, the projecting atom of 2D- C_s -1 is less strongly bound and deforms

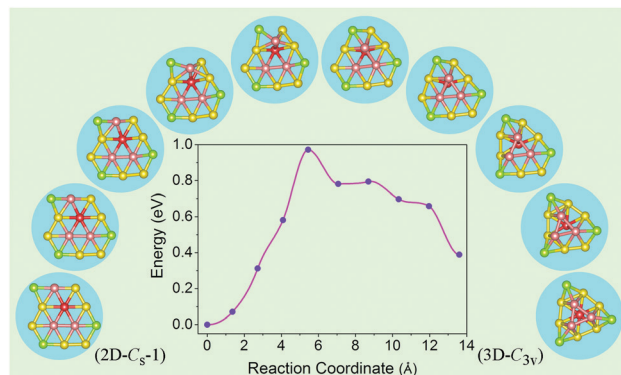


Fig. 3 Detailed pathway linking the 2D and 3D structures of Au_{13} with selected images in the transition. The atoms of the images are colored according to their relative positions in 3D- C_{3v} .

initially in the transformation, leading to the bulging out of one of its neighboring atoms, and the following structural deformation. The pathway has a fairly low barrier of 0.976 eV, linking the 2D and 3D cluster funnels.

4 Conclusions

In summary, an efficient approach is presented to screen for trial pathways between vastly different configurations, irrespective of the underlying mechanics and based on the atomic configurations only. A study about Au_{13} shows that on the basis of a configuration space the structures can be arranged and projected on a 2D map revealing the energy landscape visually. Typically, the 2D and 3D clusters get together respectively due to their similar structures and lower corresponding barriers, forming two corrugated basins in the high-dimensional configuration space. As the 2D map demonstrates, configurations 2D- C_s -1 and 3D- C_{3v} are relatively similar with a transition pathway with a fairly low barrier of 0.976 eV linking the two basins.

Conflicts of interest

There are no conflicts to declare.

Acknowledgements

This work is financially supported by NSFC (Grant No. 11574088 and 51431001), the Foundation for Innovative Research Groups of the National Natural Science Foundation of China (Grant No. 51621001), and Natural Science Foundation of Guangdong Province of China (Grant No. 2016A030312011).

References

- 1 D. J. Wales and J. P. K. Doye, *J. Phys. Chem. A*, 1997, **101**, 5111–5116.
- 2 R. Martoňák, A. Laio and M. Parrinello, *Phys. Rev. Lett.*, 2003, **90**, 075503.

- 3 A. R. Oganov and C. W. Glass, *J. Chem. Phys.*, 2006, **124**, 244704.
- 4 Y. Wang, J. Lv, L. Zhu and Y. Ma, *Comput. Phys. Commun.*, 2012, **183**, 2063–2070.
- 5 W. Setyawan and S. Curtarolo, *Comput. Mater. Sci.*, 2010, **49**, 299–312.
- 6 A. Jain, G. Hautier, C. J. Moore, S. Ping Ong, C. C. Fischer, T. Mueller, K. A. Persson and G. Ceder, *Comput. Mater. Sci.*, 2011, **50**, 2295–2310.
- 7 G. Hautier, C. C. Fischer, A. Jain, T. Mueller and G. Ceder, *Chem. Mater.*, 2010, **22**, 3762–3767.
- 8 B. Meredig, A. Agrawal, S. Kirklin, J. E. Saal, J. W. Doak, A. Thompson, K. Zhang, A. Choudhary and C. Wolverton, *Phys. Rev. B: Condens. Matter Mater. Phys.*, 2014, **89**, 094104.
- 9 H. Eyring, *J. Chem. Phys.*, 1935, **3**, 107–115.
- 10 G. Henkelman and H. Jónsson, *J. Chem. Phys.*, 2000, **113**, 9978–9985.
- 11 G. Henkelman, B. P. Uberuaga and H. Jónsson, *J. Chem. Phys.*, 2000, **113**, 9901–9904.
- 12 D. J. Wales, *J. Chem. Phys.*, 1994, **101**, 3750–3762.
- 13 G. Henkelman and H. Jónsson, *J. Chem. Phys.*, 1999, **111**, 7010–7022.
- 14 C. Dellago, P. G. Bolhuis, F. S. Csajka and D. Chandler, *J. Chem. Phys.*, 1998, **108**, 1964–1977.
- 15 C. Dellago, P. G. Bolhuis and D. Chandler, *J. Chem. Phys.*, 1998, **108**, 9236–9245.
- 16 P. G. Bolhuis, D. Chandler, C. Dellago and P. L. Geissler, *Annu. Rev. Phys. Chem.*, 2002, **53**, 291–318.
- 17 D. J. Wales, *Mol. Phys.*, 2002, **100**, 3285–3305.
- 18 O. M. Becker and M. Karplus, *J. Chem. Phys.*, 1997, **106**, 1495–1517.
- 19 D. J. Wales, M. A. Miller and T. R. Walsh, *Nature*, 1998, **394**, 758.
- 20 X.-T. Li, X.-B. Yang and Y.-J. Zhao, *J. Chem. Phys.*, 2017, **146**, 154108.
- 21 X.-T. Li, S.-G. Xu, X.-B. Yang and Y.-J. Zhao, *J. Chem. Phys.*, 2017, **147**, 144106.
- 22 P. Pyykkö, *Angew. Chem., Int. Ed.*, 2004, **43**, 4412–4456.
- 23 P. Pyykkö, *Chem. Soc. Rev.*, 2008, **37**, 1967–1997.
- 24 H. Häkkinen, M. Moseler and U. Landman, *Phys. Rev. Lett.*, 2002, **89**, 033401.
- 25 E. M. Fernández, J. M. Soler and L. C. Balbás, *Phys. Rev. B: Condens. Matter Mater. Phys.*, 2006, **73**, 235433.
- 26 W. Fa, C. Luo and J. Dong, *Phys. Rev. B: Condens. Matter Mater. Phys.*, 2005, **72**, 205428.
- 27 L. Xiao, B. Tollberg, X. Hu and L. Wang, *J. Chem. Phys.*, 2006, **124**, 114309.
- 28 B. Assadollahzadeh and P. Schwerdtfeger, *J. Chem. Phys.*, 2009, **131**, 064306.
- 29 A. Sadeghi, S. A. Ghasemi, B. Schaefer, S. Mohr, M. A. Lill and S. Goedecker, *J. Chem. Phys.*, 2013, **139**, 184118.
- 30 B. K. P. Horn, *J. Opt. Soc. Am. A*, 1987, **4**, 629–642.
- 31 K. S. Arun, T. S. Huang and S. D. Blostein, *IEEE Trans. Pattern Anal. Mach. Intell.*, 1987, **9**, 698–700.
- 32 T. F. Havel, I. D. Kuntz and G. M. Crippen, *Bull. Math. Biol.*, 1983, **45**, 665–720.
- 33 H. W. Kuhn, *Naval Res. Logist. Q.*, 1955, **2**, 83–97.
- 34 G. Kresse and D. Joubert, *Phys. Rev. B: Condens. Matter Mater. Phys.*, 1999, **59**, 1758–1775.
- 35 G. Kresse and J. Furthmüller, *Phys. Rev. B: Condens. Matter Mater. Phys.*, 1996, **54**, 11169–11186.
- 36 J. P. Perdew, K. Burke and M. Ernzerhof, *Phys. Rev. Lett.*, 1996, **77**, 3865–3868.
- 37 J. Wang, G. Wang and J. Zhao, *Phys. Rev. B: Condens. Matter Mater. Phys.*, 2002, **66**, 035418.
- 38 S. Bulusu and X. C. Zeng, *J. Chem. Phys.*, 2006, **125**, 154303.
- 39 J. P. Perdew, K. Burke and Y. Wang, *Phys. Rev. B: Condens. Matter Mater. Phys.*, 1996, **54**, 16533–16539.
- 40 P. Neogrády, V. Kellö, M. Urban and A. J. Sadlej, *Int. J. Quantum Chem.*, 1997, **63**, 557–565.